



Article

Deep Machine Learning Based Possible Atmospheric and Ionospheric Precursors of the 2021 Mw 7.1 Japan Earthquake

Muhammad Umar Draz ^{1,*}, Munawar Shah ^{1,*}, Punyawati Jamjareegulgarn ², Rasim Shahzad ¹, Ahmad M. Hasan ³ and Nivin A. Ghamry ⁴

¹ Department of Space Science, Space Education and GNSS Lab, National Center of GIS & Space Applications, Institute of Space Technology, Islamabad 44000, Pakistan

² Department of Electrical Engineering, Faculty of Engineering, King Mongkut's Institute of Technology Ladkrabang, Prince of Chumphon Campus, Chumphon 86160, Thailand; kjpunyaw@gmail.com

³ Faculty of Engineering, Future University in Egypt, Cairo 11835, Egypt

⁴ Faculty of Computers and Artificial Intelligence, Cairo University, Giza 12613, Egypt

* Correspondence: shahmunawar1@gmail.com

Abstract: Global Navigation Satellite System (GNSS)- and Remote Sensing (RS)-based Earth observations have a significant approach on the monitoring of natural disasters. Since the evolution and appearance of earthquake precursors exhibit complex behavior, the need for different methods on multiple satellite data for earthquake precursors is vital for prior and after the impending main shock. This study provided a new approach of deep machine learning (ML)-based detection of ionospheric and atmosphere precursors. In this study, we investigate multi-parameter precursors of different physical nature defining the states of ionosphere and atmosphere associated with the event in Japan on 13 February 2021 (M_w 7.1). We analyzed possible precursors from surface to ionosphere, including Sea Surface Temperature (SST), Air Temperature (AT), Relative Humidity (RH), Outgoing Longwave Radiation (OLR), and Total Electron Content (TEC). Furthermore, the aim is to find a possible pre- and post-seismic anomaly by implementing standard deviation (STDEV), wavelet transformation, the Nonlinear Autoregressive Network with Exogenous Inputs (NARX) model, and the Long Short-Term Memory Inputs (LSTM) network. Interestingly, every method shows anomalous variations in both atmospheric and ionospheric precursors before and after the earthquake. Moreover, the geomagnetic irregularities are also observed seven days after the main shock during active storm days (K_p > 3.7; Dst < −30 nT). This study demonstrates the significance of ML techniques for detecting earthquake anomalies to support the Lithosphere-Atmosphere-Ionosphere Coupling (LAIC) mechanism for future studies.

Keywords: earthquake precursors; machine learning; LAIC model; GPS TEC; coupling



Citation: Draz, M.U.; Shah, M.; Jamjareegulgarn, P.; Shahzad, R.; Hasan, A.M.; Ghamry, N.A. Deep Machine Learning Based Possible Atmospheric and Ionospheric Precursors of the 2021 Mw 7.1 Japan Earthquake. *Remote Sens.* **2023**, *15*, 1904. <https://doi.org/10.3390/rs15071904>

Academic Editors: Kwangsun Ryu and Jian Kong

Received: 6 February 2023

Revised: 27 March 2023

Accepted: 31 March 2023

Published: 2 April 2023



Copyright: © 2023 by the authors. Licensee MDPI, Basel, Switzerland. This article is an open access article distributed under the terms and conditions of the Creative Commons Attribution (CC BY) license (<https://creativecommons.org/licenses/by/4.0/>).

1. Introduction

Earthquakes cause intense shaking of the Earth's surface, with the earthquakes being the result of the brittle failure of the lithosphere. The 21st century has brought an evaluation to the field of satellite measurements, especially for earthquake precursors. Many researchers have observed anomalies prior to major earthquakes over the epicenter at different altitudes with various GNSS and RS satellites during the seismogenic period [1–7]. These short-term anomalies can be observed from 2 to 20 days before and 10 days after the main event, but still, no one presented a legitimate earthquake anomaly. Interestingly, these anomalies show positive and negative deviations beyond the defined bounds and are not only limited to the surface but these can also be observed in the ionosphere and atmosphere [8]. The lithosphere encounters various geophysical changes and as a result, these changes, precursors occurred over the earthquake epicenter [9]. In general, earthquake precursors are categorized into three different types; surface precursors, such as land surface temperature and SST, atmospheric precursors, such as OLR, RH, AT [5], and

ionospheric precursors, such as TEC, electric field disturbance, and high energy particle flux [10–13]. The propagation of earthquake anomalies from the lithosphere to ionosphere can be defined by the LAIC hypothesis [9]. There is also another theory that correlates the ionosphere and atmosphere precursors with the impending main shock (i.e., Positive holes (p-holes)). During the earthquake preparation period, stressed rocks release p-holes that result in the formation of the electric current and consequently emit electromagnetic radiations that move upward to create vulnerability in the ionosphere [14]. Furthermore, the idea of radon emission from the epicentral region also gained importance for the presentation of earthquake anomalies by air ionization near the Earth's surface, followed by emanation to the atmosphere and ultimately rising to the ionosphere [9]. In the epicentral region, emission of gases, such as radon, from the deformation of rocks due to tectonic stress can cause atmospheric anomalies. Moreover, ionospheric anomalies related to seismic activity over the epicenter are also reported by GNSS TEC. However, no clear ionospheric anomalies were observed by studying ionospheric anomalies around the 1279 earthquakes of $M_w \geq 6$ during the time period of 2000–2014 [15]. Still, there are many well-published studies about the atmospheric and ionospheric anomalies associated with earthquakes. For example, both positive and negative TEC anomalies are detected by utilizing statistical analysis on ground receiver data for the M_w 7.8 Nepal earthquake [16]. Furthermore, significant TEC variations were also observed before and after the 2014 M_w 6.9 Samothrace earthquake [17]. An anomalous variation of more than 30 W/m^2 was observed in OLR for the Japan earthquakes and other events [5,18–21]. The reflection, emission, and absorption of OLR are due to a complicated system of aerosols, clouds, ocean surface temperature, and land surface temperature variations during the main shock preparation period [22]. Both the negative and positive anomalies are observed in the SST variable, which is considered to be the most important atmospheric precursor [23]. The emission of radon resulted in anomalous variations of AT and RH over the epicenter, as explained in the LAIC model [9]. Similarly, stress and tectonic blocks' movement activate the thermodynamics phenomena and ionization process that result in the anomalous variations of AT and RH. Recent earthquakes showed clear enhancement in the atmospheric and ionospheric variations associated with main shocks [24–32]. GNSS and RS have played a vital role in understanding and finding the variations in atmospheric and ionospheric parameters from various space observations and ground stations [33–37]. The use of different algorithm on time series data is also very common these days [38–42]. Nevertheless, there is a gigantic gap of applications and knowledge related to the science of earthquake precursors.

In this paper, we have studied possible ionospheric and atmospheric anomalies associated with the M_w 7.1 Namie, Japan earthquake by implementing statistical as well as machine learning procedures (NARX and LSTM) on TEC and other remote sensing indices, including RH, OLR, and SST. The main aim is to find a synchronized window of the atmospheric and ionospheric anomalies within the same occurrence days. Moreover, another aim is to find the presence of pre-and/or post-seismic anomalies. The structure of this paper is as follows: Study area and brief description of earthquake data are described in Sections 2 and 3, respectively. Methodology is explained in Section 4. Results are described in Section 5. Discussion is explained in Section 6. Section 7 is dedicated to the conclusion.

2. Study Area

A strong earthquake of M_w 7.1 struck the east coast of Honshu, Japan on 13 February 2021, at 14:07:49 UTC (LT = UTC + 09:00 = 23:07:49). The epicenter was located at 73 km of Namie, Japan (37.7°N , 141.7°E). The United States Geological Survey (USGS) announced the maximum felt intensity of IX (heavy) and shaking intensity of VIII (severe) on a modified Mercalli scale. One person died in Fukushima and around 187 people were injured. There was a massive destruction to property with an approximate value of the damages being 9137 houses and 311 schools. The earthquake occurred as a result of thrust faulting near the subduction zone interface plate boundary between the North American and Pacific plates (Figure 1). Subduction was beneath the Japan Trench. The Pacific plate moves westward

relative to the North America plate, at a velocity of 70 mm/yr. The several micro plates in this region describe the relative motions among Pacific, North American, and Eurasian plates. The February 13, 2021 earthquake struck in the vicinity of the rapture area of the March 11, 2011 great Tohoku earthquake, which was widely felt along many islands of Japan and killed almost 16,000 people. The epicenter of the February 13 earthquake was located approximately 74 km from the epicenter of the Tohoku earthquake. After the March 2011 M_w 9.1 Tohoku earthquake, six earthquakes of $M_w > 7$ have occurred within 250 km of the February 13 earthquake. The USGS website contains more tectonic and technical information about this earthquake (<https://earthquake.usgs.gov/earthquakes/eventpage/us6000dher/executive>; accessed on 11 November 2022).

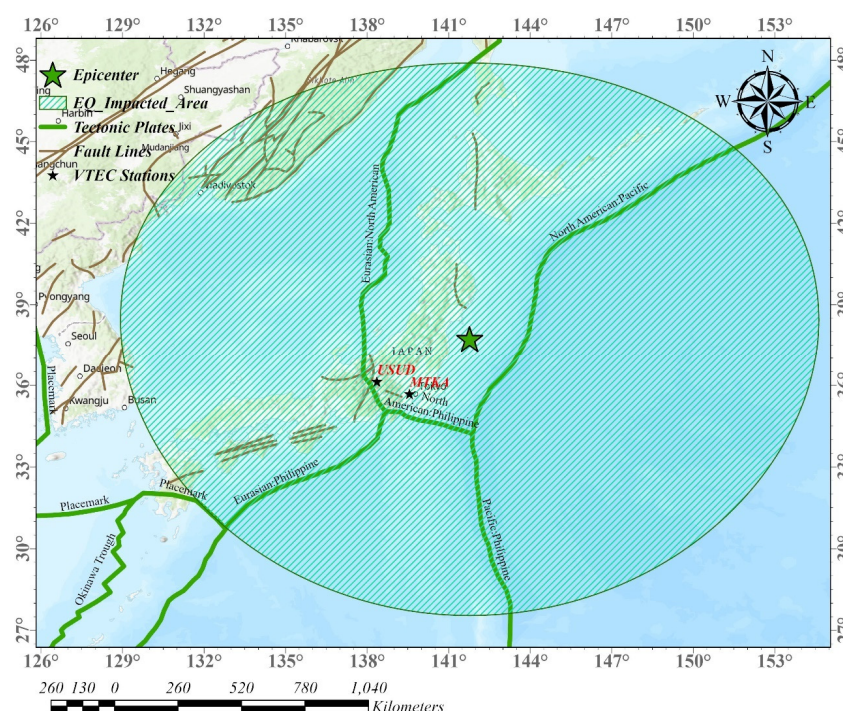


Figure 1. Geographical location of the 2021 M_w 7.1, Japan earthquake (Lat = 37.7°N, Long = 141.7°E) with tectonic plates and fault lines. The epicenter is indicated by the green star and the GNSS stations are indicated by black stars and the shaded circle area is the earthquake-impacted area estimated by the Dobrovolsky formula.

3. Materials and Datasets

3.1. Outgoing Longwave Radiation

OLR is one of the most vital parameters used to define the Earth's radiation emitted from the earthquake regions. The OLR is a combination of emissions from clouds, the lower atmosphere, ground, which have been used to investigate Earth's radiative climate [43–46]. The OLR (W/m^2) data for both the day and night are acquired at spatial resolution of 1° of AIRS/Aqua from Goddard Earth Sciences Data and Information Services Center (GES DISC). The area averaged data of OLR time series covering the earthquake epicenter within a seismogenic area ($139.4^\circ E$ – $143.9^\circ E$, $35.6^\circ N$ – $39.5^\circ N$) was retrieved from GIOVANNI with a web-based application developed by (GES DISC).

3.2. Relative Humidity

The RH is the ratio of the actual measured water vapor in the air to the saturation vapor pressure at a specific temperature. The main purpose of RH is to study the global energy budget, atmospheric dynamics, climate response related to earthquakes, and troposphere-stratosphere exchange over the epicenter. We study the RH data for both daytime and nighttime from AIRS/Aqua (GES DISC), GIOVANNI.

3.3. Air Temperature

AT indicates response of seismic activity in atmosphere and is used to understand the atmospheric phenomena related to main shock. AT (K) data is acquired from the National Oceanic and Atmospheric Administration (NOAA) at the spatial resolution of $2.5^\circ \times 2.5^\circ$ along latitude \times longitude. Moreover, some AT data was also retrieved from the National Centers for Environmental Prediction (NCEP)/National Center for Atmospheric Research (NCAR) reanalysis project.

3.4. Sea Surface Temperature

SST is one of the most significant variables used to figure out air-sea interaction and climate scenario over the epicenter. SST ($^\circ\text{C}$) data was obtained from the Modern Resolution Imaging Spectroradiometer (MODIS) AQUA/ASMR-E Satellite. MODIS SST data have a very remarkable correlation with previous research for air-surface temperature information associated with future earthquakes.

3.5. Total Electron Content

In this paper, we also retrieved TEC from three IGS stations (USUD, MTKA, and HYDE). Two stations, USUD and MTKA (Japan), are operating in the earthquake breed zone, while the third station, HYDE (India), is outside of the earthquake-affected zone. We analyzed TEC data from the HYDE station to confirm the ionospheric anomalies of the geomagnetic storm and distinguish them from the earthquake ionospheric anomalies. The GPS TEC from these stations is retrieved via (<http://www.ionolab.org/index.php?page=index&language=en>; accessed on 21 November 2022). The GPS TEC values before and after the earthquake were examined in the earthquake preparation zone in the form of vertical TEC (VTEC). Moreover, VTEC values were obtained from Slant TEC (STEC) and examined in the TEC unit ($1 \text{ TECU} = 10^{16} \text{ el/m}^2$). The STEC values were used to calculate the VTEC values, as shown below [47].

$$STEC_a^h = \frac{-(f_1^2 f_2^2)}{40.3(f_1^2 - f_2^2)} \left(P_{(4,a)}^h - c.DCB_a - c.DCB^h \right) \quad (1)$$

$$VTEC = STEC \times \cos \left[\arcsin \left(\frac{R \sin z}{R + H} \right) \right] \quad (2)$$

where (f_1^2, f_2^2) are the dual frequencies received at the GPS stations, $P_{(4,a)}^h$ is the difference between the smoothed coded measurements, c is the speed of light, DCB^h and DCB_a are differential code biases for GPS and satellite receiver, respectively. Similarly, R is the Earth's radius, z is the zenith angle of satellite, and H is the ionospheric height.

4. Methodology

We examined ionospheric and atmospheric data of 1 month (i.e., 20 days before and 10 days after) over the epicenter in earthquake breeding zone within the Dobrovolsky region [48]. For any earthquake, the stress radius (km) can be calculated by the following equation:

$$R = 10^{0.43M} \quad (3)$$

where, R and M are the preparation zone and magnitude of the earthquake, respectively. Furthermore, the earthquake magnitude value affects the radius of the breeding zone; i.e., a large magnitude earthquake has larger stress radius and vice versa. The radius of the Japan earthquake is approximately 1130 km, as calculated by the Dobrovolsky formula.

4.1. Anomaly Detection Using Statistical Method

We calculated the confidence bounds based on the mean (M) and standard deviation (STDEV) to check and validate the any deviations in the atmospheric datasets for seismic influence. These confidence bounds (lower and upper) were obtained from the mean

and standard deviation of all the values before and after the main shock by the below equations [10]:

$$UB = M + 1.6 * (STDEV) \quad (4)$$

$$LB = M - 1.6 * (STDEV) \quad (5)$$

The above equations declared that the calculated values falling outside these bounds will be considered as abnormal seismic values. The * is for multiplication.

4.2. Anomaly Detection Using Wavelet Transformation

To further validate the anomalous variations of the surface and atmospheric parameters, the wavelet transformation has been implemented on the OLR, AT, RH, and SST time series data of earthquakes.

$$(\omega_{\Psi})(y, z) = \frac{1}{\sqrt{y}} \int_{-\infty}^{+\infty} f(x) \Psi^* \left[\frac{x-z}{y} \right] dx \quad (6)$$

where, $f(x)$ is the time series under analysis and Ψ^* is the complex conjugate of continuous wavelet function. Similarly, y and z are the scaling factor and location parameter, respectively. In this study, $M \pm 1.6(STDEV)$ has been selected as the optimum threshold value to detect the unusual values of the wavelet coefficients for the Japan earthquake. The anomalies outside the confidence bounds can be related to main shock.

4.3. Anomaly Detection Using Artificial Neural Network (ANN)

ANN has offered a promising technique for the time series forecasting. Various successful applications of this method proved that ANN can be very effective in the forecasting and modeling of non-linear time series [49,50]. ANN uses a complicated connection between the input and output parameters to show the anomalous pattern in the data. In this study, we input ANN as obtained values, mean values, deviation from mean values, upper and lower bounds values, and deviation from bounds values. Moreover, the anomalies in atmospheric parameters were observed based on the comparison between the observed and ANN predicted values.

4.4. Nonlinear Autoregressive Network with Exogenous Inputs (NARX)

The NARX model is widely used in time series modeling with feedback connections enclosing various layers of the network. The dependent output signal $y(t)$ estimation is regressed against both the independent input signal and the output signal in the NARX network architecture used to represent the time series. The NARX model-defining equation is below.

$$y(t) = f(y(t-1), y(t-2), \dots, y(t-n_y), x(t-1), x(t-2), \dots, x(t-n_x)) \quad (7)$$

The network architecture and training estimation error were established repeatedly by acquiring the output, input delays, hidden layer count, related neurons, activation functions, and learning method. The function f is a nonlinear function. To implement the prediction process, N observations (y_1, y_2, \dots, y_N) were selected as the training set and the remaining ones ($y_{N+1}, y_{N+2}, \dots, y_{N+m}$) were considered to be the test set. In this study, a projected network was constructed consisting of six nodes in the input layer, 10 in the first and second hidden layers, and one in the output layer. The observed time series data, respective time, mean value, and deviation of observed time series data from the mean distribution are considered to be inputs. A time series of daily values are displayed within the Dobrovolsky region as the output layer. The training patterns in the proposed network are as follows:

$$y_4 = f(y_1, y_2, y_3, t_1, t_2, t_3) \quad (8)$$

$$y_5 = f(y_2, y_3, y_4, t_2, t_3, t_4) \quad (9)$$

$$y_N = f(y_{N-3}, y_{N-2}, y_{N-1}, t_{N-3}, t_{N-2}, t_{N-1}) \quad (10)$$

Finding optimum weights that reduce prediction error (PE) is often how prediction performance is assessed. The PE equation appears as follows:

$$PE = \sum_{k=0}^N (\hat{y}(t-k) - y(t-k)) \quad (11)$$

where \hat{y} represents the output of the network. The testing patterns are:

$$y_{N+4} = f(y_{N+1}, y_{N+2}, y_{N+3}, t_{N+1}, t_{N+2}, t_{N+3}) \quad (12)$$

$$y_{N+5} = f(y_{N+2}, y_{N+3}, y_{N+4}, t_{N+2}, t_{N+3}, t_{N+4}) \quad (13)$$

$$y_{N+m} = f(y_{N+m-3}, y_{N+m-2}, y_{N+m-1}, t_{N+m-3}, t_{N+m-2}, t_{N+m-1}) \quad (14)$$

Finally, the deviations were calculated by comparing the variations between the actual and the predicted values crossing the pre-defined bounds.

4.5. Long Short-Term Memory (LSTM)

The LSTM model can analyze the dynamic temporal pattern in time series data while running through time. A closed layer of the LSTM has three units (output, input, and nine forget) to conduct the flow of information to the memory cell. The mathematical functions of the three units are as follows:

$$i_u = \sigma(W_i x_t + W_{H_i} H_{t-1} + b_i) \quad (15)$$

$$f_u = \sigma(W_f x_t + W_{H_f} H_{t-1} + b_f) \quad (16)$$

$$o_u = \sigma(W_o x_t + W_{H_o} H_{t-1} + b_o) \quad (17)$$

$$c_t = c_{t-1} \otimes (f_u)_t + (i_u)_t \otimes \tanh(W_c x_t + W_{H_c} H_{t-1} + b_c) \quad (18)$$

$$H_t = o_t \otimes \tanh(c_{t-1}) \quad (19)$$

$$y_t = H_t \quad (20)$$

The above equations illustrate input unit, forget unit, output unit, current memory cell unit, hidden unit, and output cell, respectively, at time t . The kernel functions are represented by σ and \tanh , whereas H_{t-1} denotes the previously hidden unit and c_t shows the current cell unit. Moreover, b and W indicate bias variables and weight matrices of three units and memory cell units, respectively. Similarly, \otimes indicates the element-wise multiplication between the output, input, and cell units of closed layers.

5. Results

In this study, we analyzed multiple atmospheric and ionospheric datasets for possible earthquake precursors by various statistical as well as ML methods before and after the Japan earthquake. The resulting anomalies are discussed in detail.

5.1. Outgoing Longwave Radiation

We studied the variations in both daytime and nighttime OLR values over the epicenter of the Japan earthquake (Figure 2). The time series analysis of OLR daytime showed immense deviations over the epicenter with considerable anomalies prior to the Japan earthquake. There was an obvious positive anomaly of 36 W/m^2 on six days before the earthquake (Figure 2a).

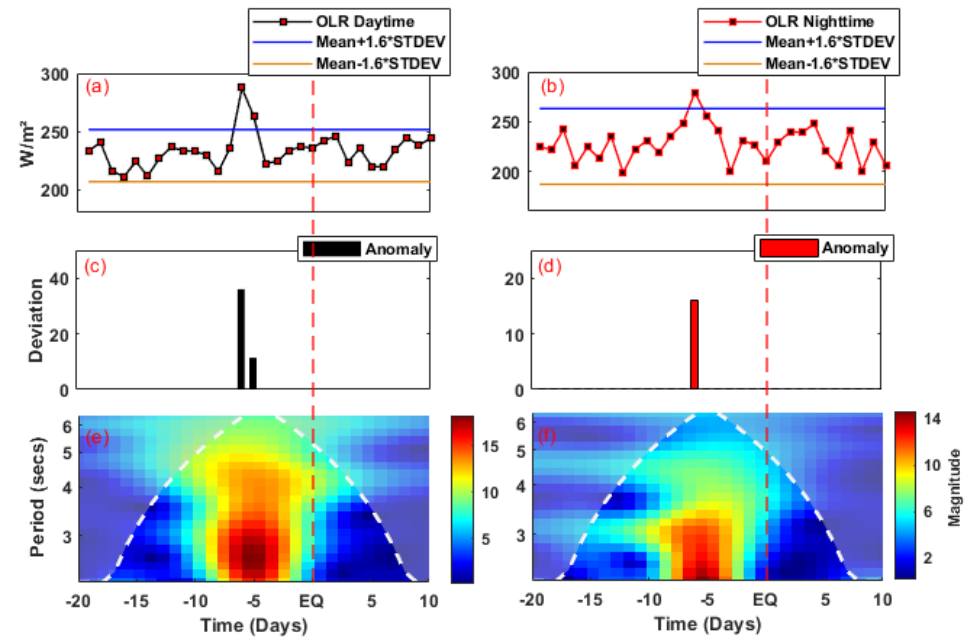


Figure 2. (a) Daytime OLR averaged time series data with confidence bounds, (b) Time series data of OLR nighttime with confidence bounds, (c) The deviation of daytime OLR values from confidence bounds, (d) Nighttime OLR deviation from the confidence bounds, (e) Wavelet transformation of the daytime OLR time series data, (f) Wavelet transformation analysis of nighttime OLR time series data. The white dashed line marks cone of influence and red dashed line shows the earthquake day. The * is for multiplication.

Similarly, a positive anomaly of 11.4 W/m^2 was also observed on the fifth day before the main shock. The time series analysis of OLR nighttime also showed a positive anomaly of 16 W/m^2 on the sixth day before the earthquake (Figure 2b). On the other hand, the wavelet transformation method implemented on OLR values for daytime and nighttime has demonstrated more evidence about the earthquake-induced anomalies. A clear OLR daytime anomaly of high magnitude occurred on the sixth and fifth days before the main shock (Figure 2e) and a significant nighttime OLR on the fifth day before the main shock (Figure 2f). Moreover, the deviations of NARX-predicted OLR daytime values showed clear anomalies within the five-day window before the seismic event (Figure 3c). Figure 3g showed a clear variation in LSTM-predicted OLR daytime values within the five-day window before the main event. NARX- and LSTM-predicted OLR nighttime values also endorse the anomalies within the 10-day window of the pre-seismic event (Figure 3d–h).

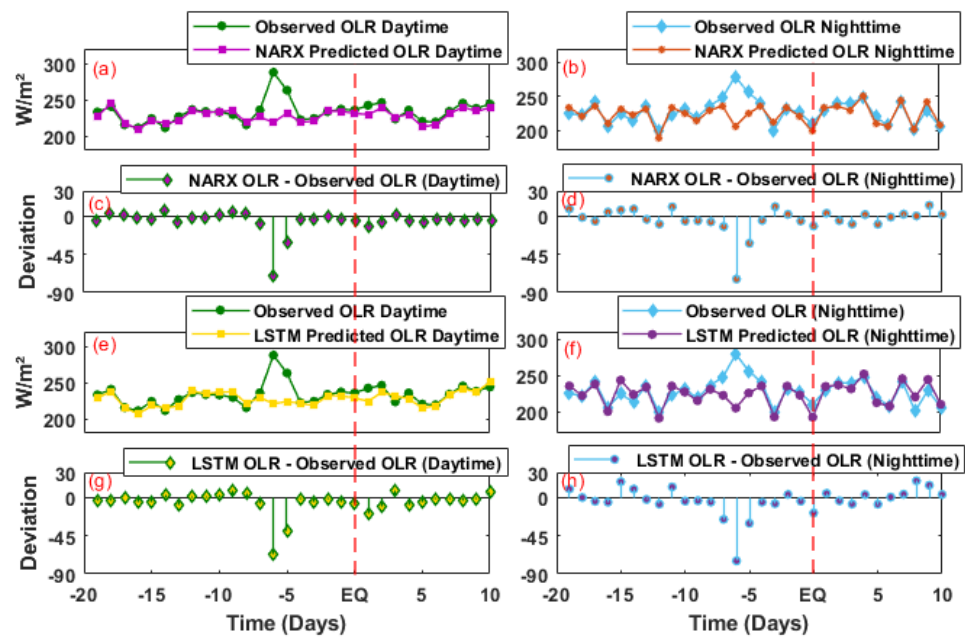


Figure 3. (a) Time series data variations between the observed OLR daytime values and NARX-predicted OLR daytime values, (b) Nighttime variations between the observed OLR values and NARX-predicted OLR, (c) Deviation of NARX-predicted OLR daytime values from the observed daytime OLR values, (d) Deviation of NARX-predicted OLR nighttime values from the observed nighttime OLR values, (e) Time series data variations between the observed OLR daytime values and LSTM train OLR daytime values, (f) Nighttime variations between observed OLR values and LSTM train OLR, (g) Deviation of LSTM-predicted OLR daytime values from Observed daytime OLR values, (h) Deviation of LSTM-predicted OLR nighttime values from Observed daytime OLR values. The red dashed line shows earthquake day.

5.2. Relative Humidity

The RH data for both daytime and nighttime are evaluated to observe the variations prior to the Japan event. Time series analysis of the RH daytime values showed a negative anomaly of -8% on the sixth day before the main earthquake day (Figure 4a). Analysis of RH nighttime values also showed a negative anomaly below the bound of $\text{Mean} - 1.6 \cdot \text{STDEV}$ of -6% on the fifth day prior to the main shock (Figure 4b). We also noticed sharp variation in the continuous wavelet transformation in both daytime and nighttime RH values of high magnitude within the 10-day window prior to the main shock (Figure 4e,f). NARX- and LSTM-predicted RH daytime values showed a clear negative anomaly on the sixth day before the event (Figure 5c–g). Moreover, Figure 5 showed clear deviations on the sixth and fifth day before the earthquake for both NARX- and LSTM-predicted values in nighttime RH.

5.3. Air Temperature

In this paper, we also studied the AT values of the Japan earthquake, which showed a clear positive anomaly on the fifth day before the main shock (Figure 6a). Moreover, an obvious positive anomaly also occurred beyond the $\text{Mean} + 1.6 \cdot \text{STDEV}$ bound on 8th February with a deviation of 2K. The continuous wavelet transformation showed a variation of high magnitude within the five-day period before the main earthquake (Figure 6c). NARX- and LSTM-predicted AT values also showed clear anomalies within five days before the main shock day (Figure 7a–c).

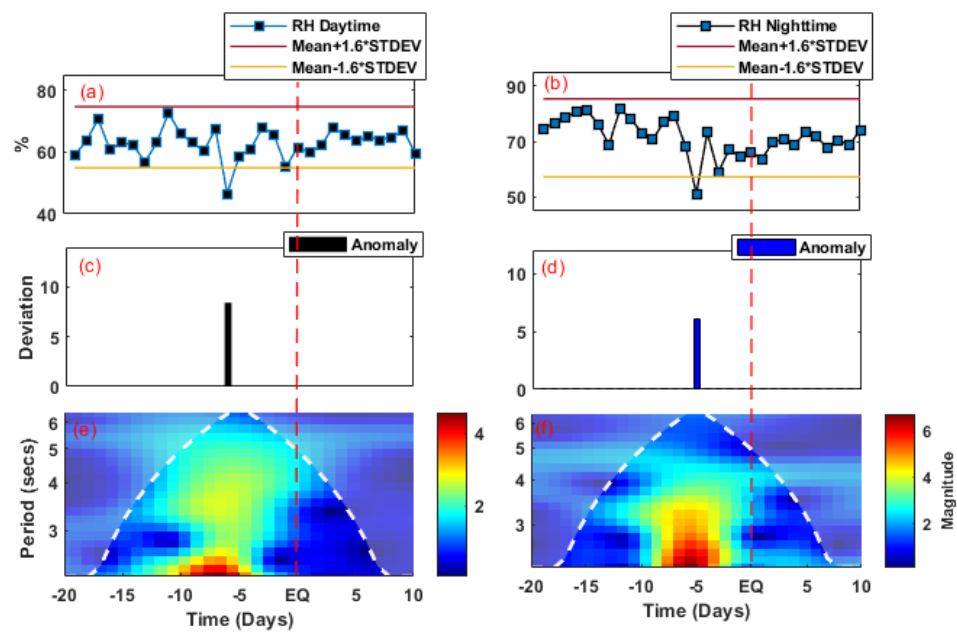


Figure 4. (a) Daytime RH averaged time series data with confidence bounds, (b) Time series data of RH nighttime with confidence bounds, (c) The deviation of daytime RH values from confidence bounds, (d) Nighttime RH deviation from pre-defined bounds, (e) Wavelet transformation of daytime RH data, (f) Wavelet transformation analysis of nighttime RH time series data. The white dashed line in Figure 5e,f marks cone of influence and red dashed line shows the earthquake day. The * is for multiplication.

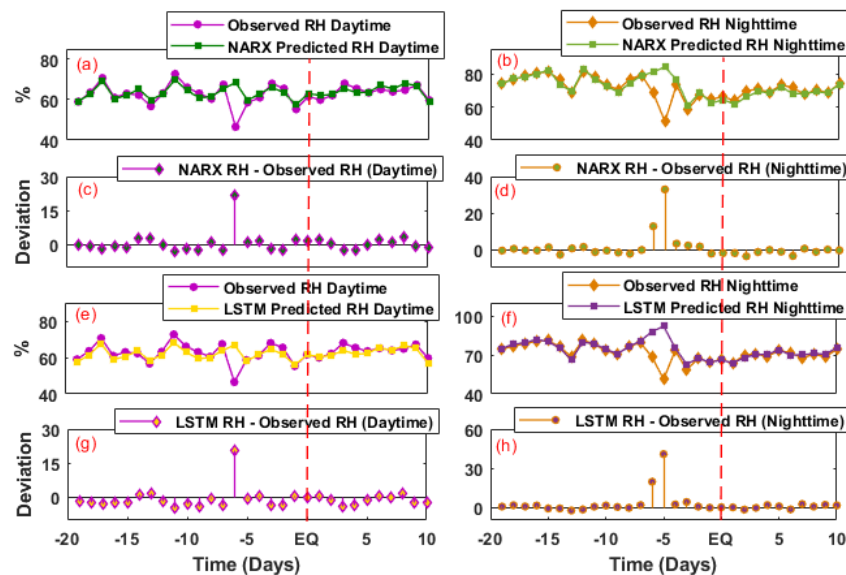


Figure 5. (a) Data variations between the observed RH daytime values and NARX-predicted RH daytime values, (b) Nighttime variations between the observed RH values and NARX-predicted RH, (c) Deviation of NARX-predicted RH daytime values from Observed daytime RH values, (d) Deviation of NARX-predicted RH nighttime values from Observed nighttime RH values, (e) Time series data variations between observed RH daytime values and LSTM train RH daytime values, (f) Nighttime variations between observed RH values and LSTM train RH, (g) Deviation of LSTM-predicted RH daytime values from Observed daytime RH values, (h) Deviation of LSTM-predicted RH nighttime values from Observed daytime RH values. The red dashed line shows the earthquake day.

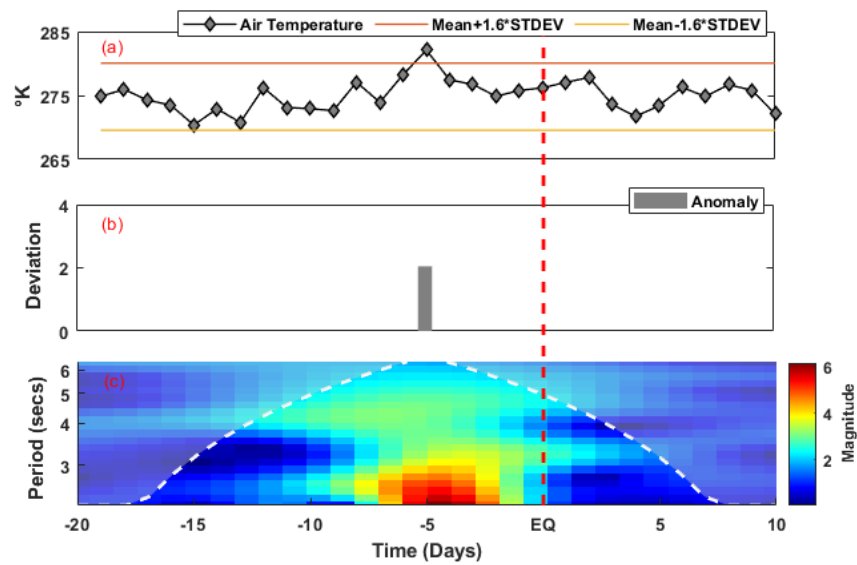


Figure 6. (a) Averaged time series data of AT with confidence bounds, (b) The deviation of AT values from confidence bounds, (c) Wavelet transformation of AT time series data. The white dashed line marks cone of influence and red dashed line shows the earthquake day. The * is for multiplication.

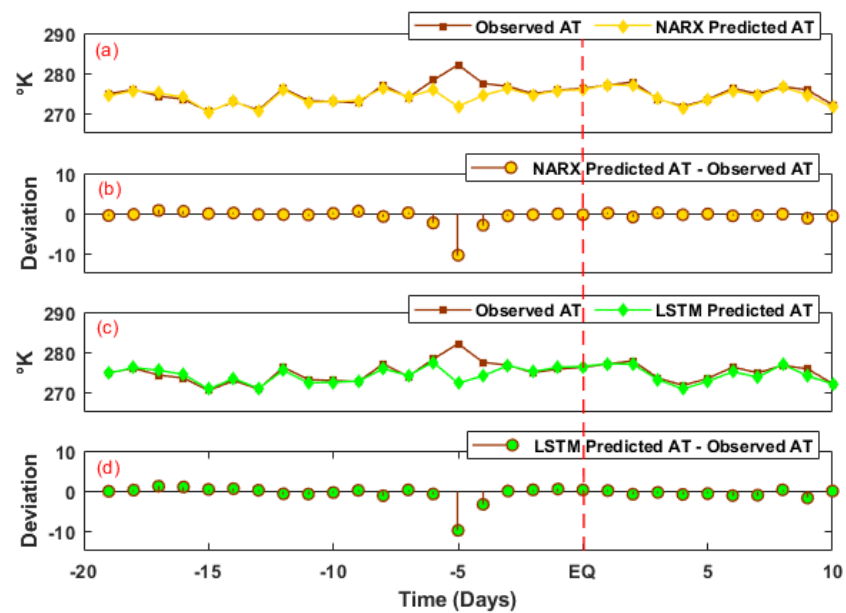


Figure 7. (a) Variations between the observed AT data and NARX-predicted AT values, (b) Deviation of NARX-predicted AT values from Observed AT values, (c) Variations between observed AT values and LSTM train AT values, (d) Deviation of LSTM-predicted AT values from Observed AT data. The red dashed line shows the earthquake day.

5.4. Sea Surface Temperature

We also studied the time series data of SST, which showed a clear negative anomaly of $-4.5\text{ }^{\circ}\text{C}$ on 7th February; i.e., six days before the earthquake (Figure 8a). This sudden decrease is observed on the sixth day before the main shock of the Japan event. Similarly, continuous wavelet transformation showed variations of high magnitude within -8 to -5 days before the earthquake, which is synchronized with the time series anomaly (Figure 8c). The comparison of NARX- and LSTM-predicted SST values with observed values also showed clear deviations -7 and -6 days prior to the main shock (Figure 9b–d).

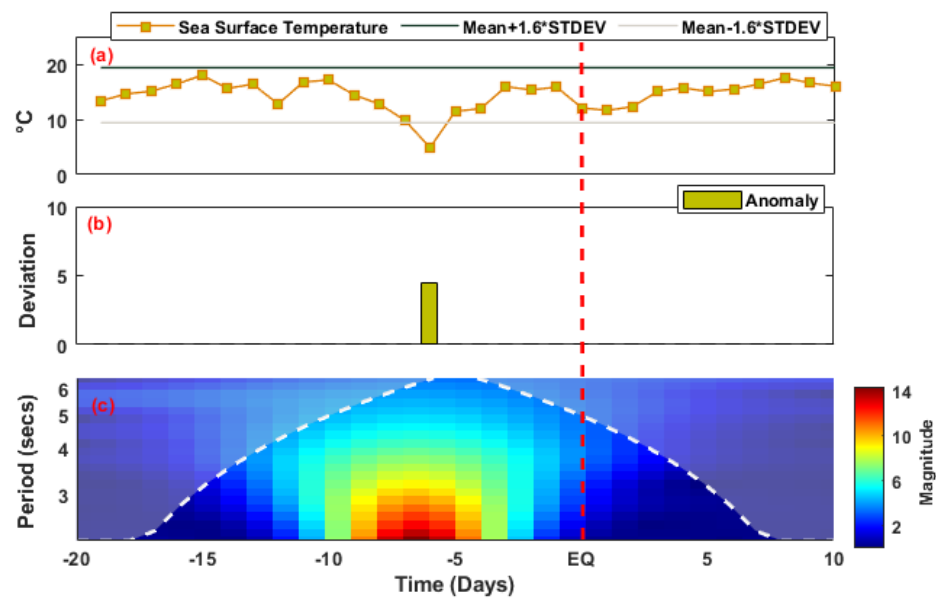


Figure 8. (a) The observation of SST data within the bounds, (b) SST data deviation from the bounds, (c) Continuous wavelet analysis of MODIS-SST time series data. The white dashed line marks cone of influence and red dashed line shows the earthquake day. The * is for multiplication.

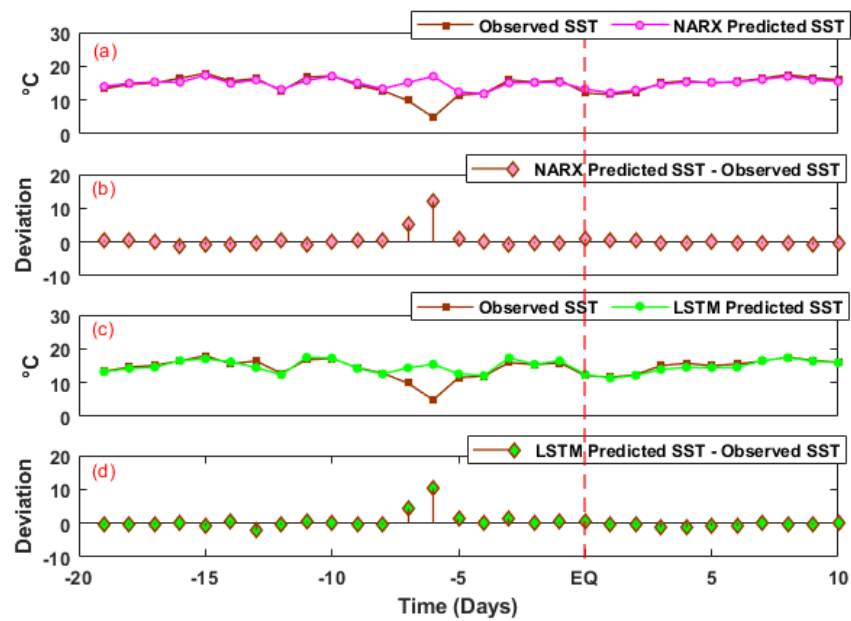


Figure 9. (a) Data variations between observed time series MODIS-SST and NARX-predicted SST values, (b) Deviation of NARX-predicted SST values from Observed SST values, (c) Variations between observed MODIS-SST values and LSTM train SST values, (d) Deviation of LSTM-predicted SST values from Observed SST data. The red dashed line shows earthquake day.

5.5. Total Electron Content

TEC data retrieved from the two IGS stations (USUD and MTKA) within the breeding zone of the M_w 7.1, Japan earthquake showed clear seismo-ionospheric anomalies. IGS station (HYDE) variation was also observed outside the seismic preparation zone to illustrate the earthquake- and storm-induced TEC anomalies. Figure 10 illustrates the associated VTEC variations recorded at two IGS stations, which operate within the seismic preparation zone. Prominent positive deviations were observed -6 and -5 days before the main shock in both USUD and MTKA stations during quiet storm days. These anomalies are synchronized with the atmospheric anomalies and occurred in the same window as atmospheric anomalies. Similarly, NARX- and LSTM-predicted values also showed clear deviations in VTEC values on the 7th and 8th February for the two IGS stations i.e., USUD and MTKA (Figures 11 and 12). USUD VTEC showed positive anomalies of 7.5 and 1.8 TECU on seven and nine days after the major event (Figure 10c). Figure 10d showed positive variations of 6.6, 1.6, and 6.7 TECU for MTKA VTEC on seven, eight, and nine days after the earthquake day, respectively. Positive TEC deviations were also observed seven and eight days after the seismic event for HYDE station (Figure 10e). During active storm days, VTEC variations for three IGS stations (USUD, MTKA, and HYDE) showed positive anomalies from 7–10 days after the earthquake day. NARX- and LSTM-predicted VTEC also showed clear deviations from 20th to 23rd February for three IGS stations during active storm days (Figures 11d and 12d). All the atmospheric and ionospheric anomalies are listed in Tables 1–3.

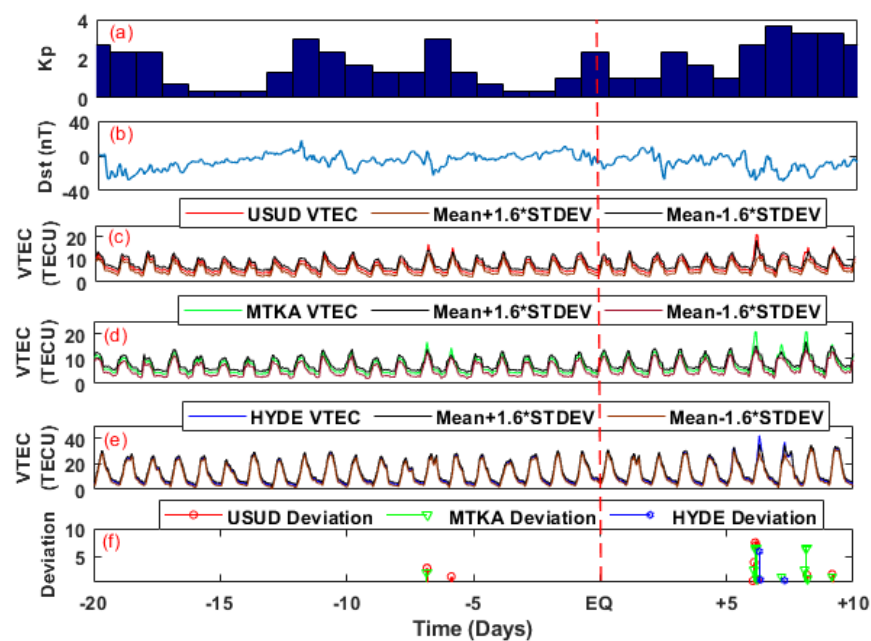


Figure 10. The solar and geomagnetic storm indices (a) Kp and (b) Dst of Japan earthquake, (c) Statistical analysis of USUD (IGS station Japan) VTEC with IQR bounds, (d) Analysis of MTKA (IGS station Japan) VTEC with pre-defined IQR bounds, (e) Time series analysis of HYDE (IGS station India) VTEC with IQR bounds, (f) Deviation of time series statistical analysis of VTEC for all available stations (USUD, MTKA, and HYDE). The red dashed line shows the earthquake day. The * is for multiplication.

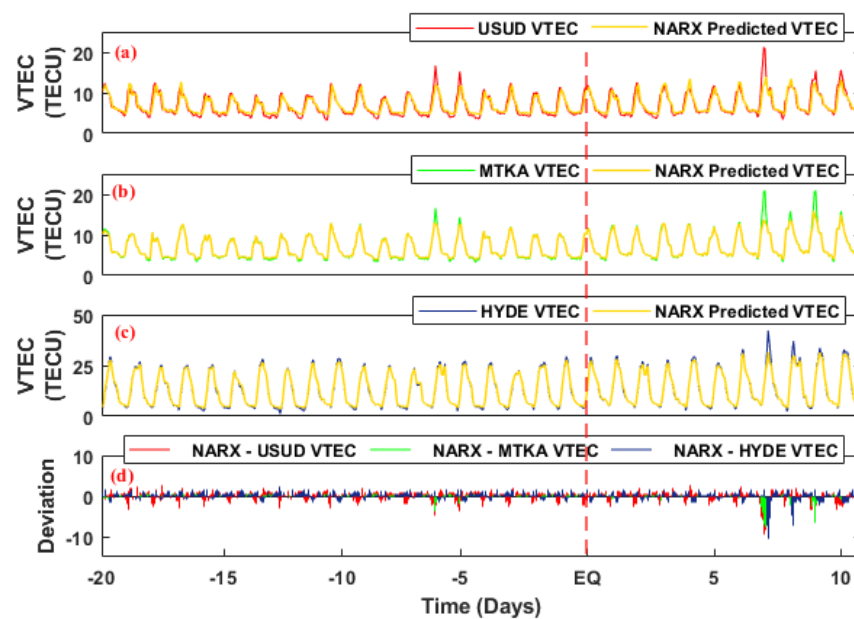


Figure 11. (a) Variation of USUD VTEC with NARX-predicted VTEC, (b) Time series variation of MTKA VTEC with NARX-predicted VTEC, (c) Variation of HYDE VTEC with NARX-predicted VTEC, (d) Deviation of NARX-predicted VTEC from USUD, MTKA, and HYDE VTEC. The red dashed line shows the earthquake day.

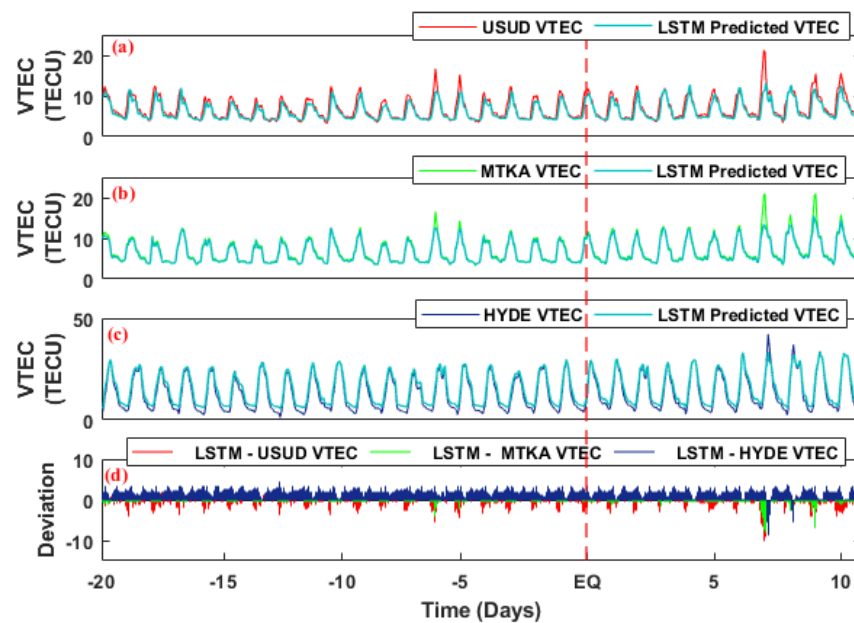


Figure 12. (a) Variation of USUD VTEC with LSTM train VTEC, (b) Time series variation of MTKA VTEC with LSTM-predicted VTEC, (c) Variation of HYDE VTEC with LSTM-predicted VTEC, (d) Deviation of LSTM train VTEC from USUD, MTKA, and HYDE VTEC. The red dashed line shows earthquake day.

Table 1. The anomalies detected using statistical method.

Parameters	Anomalous Day	Deviations from UB and LB	
		Pre-EQ	Post-EQ
OLR (Daytime)	−6, −5	36, 11.4 W/m ²	Nil
OLR (Nighttime)	−6	18 W/m ²	Nil
RH (Daytime)	−6	−8%	Nil
RH (Nighttime)	−5	−6%	Nil
AT	−5	2 °K	Nil
SST	−6	−4.5 °C	Nil
VTEC (USUD)	−6, −5, 7, 9	3, 1.5 TECU	7.5, 1.8 TECU
VTEC (MTKA)	−6, −5, 7, 8, 9	2.32, 0.5 TECU	6.6, 1.5, 6.7 TECU
VTEC (HYDE)	7, 8	Nil	5.95, 0.8 TECU

6. Discussion

In this paper, we analyzed OLR, RH, AT, SST, and TEC time series data's possible deviations within the preparation zone of the Japan earthquake. We found these anomalies due to the immense energy release during the main shock days; Ouzounov [51] showed the earthquake energy outflow towards the atmosphere. Emission of gases from the Earth's crust caused OLR anomalies, variations in AT and RH, and also resulted in air ionization, which is a notable process in the local area of active faults. There exists a strong correlation between the radon variations during the earthquake preparation period with RH, and AT in the LAI coupling over the epicenter [9,52]. There are various studies on abnormal AT resulting in lowest RH (decrease in RH due to the cooling process of hot gases emitted from the seismic region), which is a possible earthquake precursor. In this study, we also found a significant increase in OLR as a result of sudden earthquake energy release before the main shock (Figure 2), followed by abnormal decrement in RH due to emission of hot gases from the epicentral region (Figure 4). Similarly, OLR is a very important parameter and it can be efficiently used as a possible short-term earthquake precursor [52]. Similarly, rise in surface temperature can also increase OLR, specifically in the earthquake breeding zone. In this paper, daily OLR, RH, and AT deviations over the epicenter of the Japan earthquake showed anomalous behavior beyond the confidence bounds as well as with the machine learning techniques. Previous studies also suggested the decrement in RH and increment in other atmosphere indices before the earthquake [5,6,25,30,31,51,52]. However, we found synchronized and co-located atmospheric and ionospheric anomalies on the fifth and sixth days before the main shock, followed by abnormalities in the data of nearby GPS stations (Tables 1–3). The analysis in this study can be further supported by the LAIC hypothesis, which also compromised synchronized anomalies over the epicenter. Variations of OLR, RH, and AT values were also considered as evidence of seismic-induced deformation along the fault lines of seismic event regions [6,53]. SST data also showed strong evidence of disturbance around the earthquake and support of the study of other atmospheric anomalies. Therefore, this finding is consistent and compatible with previous studies [23,54,55]. There are several studies about the LAIC coupling in pre-and post-seismic effects for various events. However, some studies suggested that the earthquake-induced positive holes within the breeding zone could variant the air ionization and consequently rise the electrical conductivity [56,57]. Furthermore, Pulnits and Ouzounov [9] demonstrated that ionospheric VTEC anomalies occurrence from the radon emission of tectonic-stressed rocks during the earthquake preparation period. Additionally, high energy alpha particles, which are ionized by the initial emissions from the earthquake, could raise air conductivity by radioactive decay of the radon [7,58,59]. Moreover, the LAIC phenomenon was explained by the numerical simulations of ionospheric ionization at the lower and upper edge of the atmosphere by the induced earthquake upward electric field [60–63]. Furthermore, Kuo [60] demonstrated that the increase or decrease in ionospheric perturbations can occur only above the epicenter due to plasma flow from the epicenter. Moreover, many studies have reported several atmospheric and ionospheric anomalies within 2–3 months before and

after the earthquake by implementation of the LAIC model [64,65]. We found significant positive and negative anomalies in both atmospheric and ionospheric parameters associated with the M_w 7.1, Japan earthquake. However, there is still a need for observations and analysis for detailed calculations of different earthquake precursors.

Table 2. Detected anomalies using NARX model.

Parameters	Anomalous Day	Deviations from NARX Predicted Values	
		Pre-EQ	Post-EQ
OLR (Daytime)	−6, −5	58, 19.8 W/m ²	Nil
OLR (Nighttime)	−6, −5	48, 6 W/m ²	Nil
RH (Daytime)	−6	−15%	Nil
RH (Nighttime)	−6, −5	−6, −27%	Nil
AT	−5	8 °K	Nil
SST	−7, −6	−2.9, −9.7 °C	Nil
VTEC (USUD)	−6, −5, 7, 9	3.2, 2.9 TECU	7.6, 1.7 TECU
VTEC (MTKA)	−6, −5, 7, 8, 9	3.3, 1.48 TECU	7.3, 1.8, 6.3 TECU
VTEC (HYDE)	7, 8	Nil	9.7, 6.47 TECU

Table 3. Detected anomalies using LSTM method.

Parameters	Anomalous Day	Deviations from LSTM Predicted Values	
		Pre-EQ	Post-EQ
OLR (Daytime)	−6, −5	53.8, 26 W/m ²	Nil
OLR (Nighttime)	−6, −5	54, 9 W/m ²	Nil
RH (Daytime)	−6	−15.7%	Nil
RH (Nighttime)	−6, −5	−13.3, −34.5%	Nil
AT	−5	7 °K	Nil
SST	−7, −6	−2, −8 °C	Nil
VTEC (USUD)	−6, −5, 7, 9	3.18, 2 TECU	7.4, 2.1 TECU
VTEC (MTKA)	−6, −5, 7, 8, 9	3.23, 1.39 TECU	6.5, 1.6, 5.8 TECU
VTEC (HYDE)	7, 8	Nil	9.63, 6.32 TECU

7. Conclusions

In this paper, we have investigated the possible atmospheric and ionospheric anomalies associated with the large magnitude earthquake of M_w 7.1 in Japan from various ground-and space-measurements. The main findings are: For the daytime and nighttime analysis, the unusual variations in the atmospheric constituents beyond the confidence bounds occurred −6 and −5 days before the earthquake main shock. Moreover, the wavelet transformation and NARX and LSTM train data also endorse the anomalous behavior of atmospheric anomalies on the same days as the statistical method. The abnormal variations in OLR, SST, AT, and RH validate the coupling of the earthquake and atmosphere by the LAIC hypothesis. The sudden drop in RH confirmed the cooling of hot gases from seismogenic regions in LAIC phenomenon, followed by a sudden increase in OLR and SST due to abnormal ions and water particle drift from the lower atmosphere toward the upper atmosphere. Moreover, we also found synchronized and co-located ionosphere anomalies −6 and −5 days before the main shock with the two available stations (USUD and MTKA) within the Dobrovolsky region during quiet geomagnetic storms. All these anomalies in the atmosphere and ionosphere are due to electric field generation around the epicenter, where the charge particle propagated to the atmosphere and ionosphere via the p-hole and radon emission to form the LAIC mechanism. The statistical and ML data showed clear earthquake variations; however, more techniques are needed to develop forecasting of possible earthquake precursors from the available satellite clusters.

Author Contributions: Conceptualization, M.S.; methodology, software, M.U.D. and M.S.; validation, P.J.; writing—review and editing, R.S., A.M.H. and N.A.G. All authors have read and agreed to the published version of the manuscript.

Funding: This research is financially supported by the Academic Melting Pot of KMITL research fund (grant No. KREF206602).

Institutional Review Board Statement: Not applicable.

Acknowledgments: The authors are obliged to USGS and ISGI for providing earthquake and geomagnetic storm data. We are grateful to the IGS community for the availability of permanent GPS ground-stations. We are also thankful to GIOVANNI, NOAA, and NASA (MODIS) for providing atmospheric parameters data.

Conflicts of Interest: The authors declare no conflict of interest.

References

1. Blackett, M.; Wooster, M.J.; Malamud, B.D. Exploring land surface temperature earthquake precursors: A focus on the Gujarat (India) earthquake of 2001. *Geophys. Res. Lett.* **2011**, *38*, L15303. [[CrossRef](#)]
2. Heki, K. Ionospheric electron enhancement preceding the 2011 Tohoku-Oki earthquake. *Geophys. Res. Lett.* **2011**, *38*, L17312. [[CrossRef](#)]
3. Carter, B.A.; Kellerman, A.C.; Kane, T.A.; Dyson, P.L.; Norman, R.; Zhang, K. Ionospheric precursors to large earthquakes: A case study of the 2011 Japanese Tohoku Earthquake. *J. Atmos. Solar-Terrestrial Phys.* **2013**, *102*, 290–297. [[CrossRef](#)]
4. Shah, M.; Jin, S. Statistical characteristics of seismo-ionospheric GPS TEC disturbances prior to global Mw \geq 5.0 earthquakes (1998–2014). *J. Geodyn.* **2015**, *92*, 42–49. [[CrossRef](#)]
5. Shah, M.; Aibar, A.C.; Tariq, M.A.; Ahmed, J.; Ahmed, A. Possible ionosphere and atmosphere precursory analysis related to Mw $>$ 6.0 earthquakes in Japan. *Remote Sens. Environ.* **2020**, *239*, 111620. [[CrossRef](#)]
6. Shah, M.; Ehsan, M.; Abbas, A.; Ahmed, A.; Jamjareegulgarn, P. Possible thermal anomalies associated with global terrestrial earthquakes during 2000–2019 based on MODIS-LST. *IEEE Geosci. Remote Sens. Lett.* **2021**, *19*, 1002705. [[CrossRef](#)]
7. Shah, M.; Abbas, A.; Adil, M.A.; Ashraf, U.; de Oliveira-Júnior, J.F.; Tariq, M.A.; Ahmed, J.; Ehsan, M.; Ali, A. Possible seismo-ionospheric anomalies associated with Mw $>$ 5.0 earthquakes during 2000–2020 from GNSS TEC. *Adv. Space Res.* **2022**, *70*, 179–187. [[CrossRef](#)]
8. Venkatanathan, N.; Natyaganov, V. Outgoing longwave radiations as pre-earthquake signals: Preliminary results of 24 September 2013 (M 7.7) earthquake. *Curr. Sci.* **2014**, *106*, 1291–1297.
9. Pulnits, S.; Ouzounov, D. Lithosphere–Atmosphere–Ionosphere Coupling (LAIC) model—An unified concept for earthquake precursors validation. *J. Asian Earth Sci.* **2011**, *41*, 371–382. [[CrossRef](#)]
10. Liu, J.Y.; Chuo, Y.J.; Shan, S.J.; Tsai, Y.B.; Chen, Y.I.; Pulnits, S.A.; Yu, S.B. Pre-earthquake ionospheric anomalies registered by continuous GPS TEC measurements. *Ann. Geophys.* **2004**, *22*, 1585–1593. [[CrossRef](#)]
11. Sorokin, V.M.; Pokhotelov, O.A. Model for the VLF/LF radio signal anomalies formation associated with earthquakes. *Adv. Space Res.* **2014**, *54*, 2532–2539. [[CrossRef](#)]
12. Zhang, Z.-X.; Wang, C.-Y.; Shen, X.-H.; Li, X.-Q.; Wu, S.-G. Study of typical space wave—Particle coupling events possibly related with seismic activity. *Chin. Phys. B* **2014**, *23*, 109401. [[CrossRef](#)]
13. Aleksandrin, S.Y.; Galper, A.M.; Grishantzeva, L.A.; Koldashov, S.; Maslennikov, L.; Murashov, A.M.; Picozza, P.; Sgrigna, V.; Voronov, S.A. High-energy charged particle bursts in the near-Earth space as earthquake precursors. *Ann. Geophys.* **2003**, *21*, 597–602. [[CrossRef](#)]
14. Freund, F. Charge generation and propagation in igneous rocks. *J. Geodyn.* **2002**, *33*, 543–570. [[CrossRef](#)]
15. Thomas, J.N.; Huard, J.; Masci, F. A statistical study of global ionospheric map total electron content changes prior to occurrences of M \geq 6.0 earthquakes during 2000–2014. *J. Geophys. Res. Space Phys.* **2017**, *122*, 2151–2161. [[CrossRef](#)]
16. Shi, K.; Guo, J.; Liu, X.; Liu, L.; You, X.; Wang, F. Seismo-ionospheric anomalies associated with Mw 7.8 Nepal earthquake on 2015 April 25 from CMONOC GPS data. *Geosci. J.* **2020**, *24*, 391–406. [[CrossRef](#)]
17. Pikridas, C.; Bitharis, S.; Katsougiannopoulos, S.; Spanakaki, K.; Karolos, I.-A. Study of TEC variations using permanent stations GNSS data in relation with seismic events. Application on Samothrace earthquake of 24 May 2014. *Geod. Cartogr.* **2019**, *45*, 137–146. [[CrossRef](#)]
18. Liu, X.; Zhang, Q.; Shah, M.; Hong, Z. Atmospheric-ionospheric disturbances following the April 2015 Calbuco volcano from GPS and OMI observations. *Adv. Space Res.* **2017**, *60*, 2836–2846. [[CrossRef](#)]
19. Shah, M.; Khan, M.; Ullah, H.; Ali, S. Thermal anomalies prior to The 2015 Gorkha (Nepal) earthquake from modis land surface temperature and outgoing longwave radiations. *Geodyn. Tectonophys.* **2018**, *9*, 123–138. [[CrossRef](#)]
20. Shah, M.; Tariq, M.A.; Ahmad, J.; Naqvi, N.A.; Jin, S. Seismo ionospheric anomalies before the 2007 M7. 7 Chile earthquake from GPS TEC and DEMETER. *J. Geodyn.* **2019**, *127*, 42–51. [[CrossRef](#)]
21. Hussain, A.; Shah, M. Comparison of GPS TEC with iri models of 2007, 2012, and 1 2016 over sukkur, Pakistan. *Nat. Appl. Sci. Int. J.* **2020**, *1*, 1–10. [[CrossRef](#)] [[PubMed](#)]

22. Xiong, P.; Shen, X.H.; Bi, Y.X.; Kang, C.L.; Chen, L.Z.; Jing, F.; Chen, Y. Study of outgoing longwave radiation anomalies associated with Haiti earthquake. *Nat. Hazards Earth Syst. Sci.* **2010**, *10*, 2169–2178. [[CrossRef](#)]
23. Mohamed, E.K.; Elrayess, M.; Omar, K. Evaluation of thermal anomaly preceding northern red sea earthquake, the 16th June 2020. *Arab. J. Sci. Eng.* **2022**, *47*, 7387–7406. [[CrossRef](#)]
24. Ahmed, J.; Shah, M.; Zafar, W.A.; Amin, M.A.; Iqbal, T. Seismoionospheric anomalies associated with earthquakes from the analysis of the ionosonde data. *J. Atmos. Solar-Terrestrial Phys.* **2018**, *179*, 450–458. [[CrossRef](#)]
25. Shah, M.; Jin, S. Pre-seismic ionospheric anomalies of the 2013 Mw = 7.7 Pakistan earthquake from GPS and COSMIC observations. *Geod. Geodyn.* **2018**, *9*, 378–387. [[CrossRef](#)]
26. Tariq, M.A.; Shah, M.; Hernández-Pajares, M.; Iqbal, T. Pre-earthquake ionospheric anomalies before three major earthquakes by GPS-TEC and GIM-TEC data during 2015–2017. *Adv. Space Res.* **2019**, *63*, 2088–2099. [[CrossRef](#)]
27. Kiyani, A.; Shah, M.; Ahmed, A.; Shah, H.H.; Hameed, S.; Adil, M.A.; Naqvi, N.A. Seismo ionospheric anomalies possibly associated with the 2018 Mw 8.2 Fiji earthquake detected with GNSS TEC. *J. Geodyn.* **2020**, *140*, 101782. [[CrossRef](#)]
28. Timoçin, E.; Temuçin, H.; Inyurt, S.; Shah, M.; Jamjareegulgarn, P. Assessment of improvement of the IRI model for foF2 variability over three latitudes in different hemispheres during low and high solar activities. *Acta Astronaut.* **2021**, *180*, 305–316. [[CrossRef](#)]
29. Abbasi, A.R.; Shah, M.; Ahmed, A.; Naqvi, N.A. Possible ionospheric anomalies associated with the 2009 M w 6.4 Taiwan earthquake from DEMETER and GNSS TEC. *Acta Geod. Geophys.* **2021**, *56*, 77–91. [[CrossRef](#)]
30. de Oliveira-Júnior, J.F.; Shah, M.; Abbas, A.; Iqbal, M.S.; Shahzad, R.; de Gois, G.; da Silva, M.V.; da Rosa Ferraz Jardim, A.M.; de Souza, A. Spatiotemporal Analysis of Drought and Rainfall in Pakistan via Standardized Precipitation Index: Homogeneous Regions, Trend, Wavelet and Influence of El Niño-Southern Oscillation. *Theor. Appl. Climatol.* **2022**, *149*, 843–862. [[CrossRef](#)]
31. Khan, M.M.; Ghaffar, B.; Shahzad, R.; Khan, M.R.; Shah, M.; Amin, A.H.; Eldin, S.M.; Naqvi, N.A.; Ali, R. Atmospheric anomalies associated with the 2021 M w 7.2 Haiti earthquake using machine learning from multiple satellites. *Sustainability* **2022**, *14*, 14782. [[CrossRef](#)]
32. Tariq, M.A.; Yuyan, Y.; Shah, M.; Shah, M.A.; Iqbal, T.; Liu, L. Ionospheric-Thermospheric responses to the May and September 2017 geomagnetic storms over Asian regions. *Adv. Space Res.* **2022**, *70*, 3731–3744. [[CrossRef](#)]
33. Li, S.; Wang, F.; Wang, Q.; Ouyang, L.; Chen, X.; Li, J. Numerical Modeling of Branching-Streamer Propagation in Ester-Based Insulating Oil under Positive Lightning Impulse Voltage: Effects from Needle Curvature Radius. *IEEE Trans. Dielectr. Electr. Insul.* **2022**, *30*, 139–147. [[CrossRef](#)]
34. Roger, J.; Pelletier, B.; Aucan, J. Update of the tsunami catalogue of New Caledonia using a decision table based on seismic data and marigraphic records. *Nat. Hazards Earth Syst. Sci.* **2019**, *19*, 1471–1483. [[CrossRef](#)]
35. Wang, G.; Zhao, B.; Wu, B.; Wang, M.; Liu, W.; Zhou, H.; Han, Y. Research on the Macro-Mesoscopic Response Mechanism of Multisphere Approximated Heteromorphic Tailing Particles. *Lithosphere* **2022**, *2022*, 1977890. [[CrossRef](#)]
36. Yue, Z.; Zhou, W.; Li, T. Impact of the Indian Ocean Dipole on Evolution of the Subsequent ENSO: Relative Roles of Dynamic and Thermodynamic Processes. *J. Clim.* **2021**, *34*, 3591–3607. [[CrossRef](#)]
37. Zhong, T.; Wang, W.; Lu, S.; Dong, X.; Yang, B. RMCHN: A Residual Modular Cascaded Heterogeneous Network for Noise Suppression in DAS-VSP Records. *IEEE Geosci. Remote Sens. Lett.* **2022**, *20*, 7500205. [[CrossRef](#)]
38. Chen, Y.; Zhu, L.; Hu, Z.; Chen, S.; Zheng, X. Risk Propagation in Multilayer Heterogeneous Network of Coupled System of Large Engineering Project. *J. Manag. Eng.* **2022**, *38*, 4022003. [[CrossRef](#)]
39. Zhou, G.; Deng, R.; Zhou, X.; Long, S.; Li, W.; Lin, G.; Li, X. Gaussian Inflection Point Selection for LiDAR Hidden Echo Signal Decomposition. *IEEE Geosci. Remote Sens. Lett.* **2021**, *19*, 6502705. [[CrossRef](#)]
40. Zhou, G.; Bao, X.; Ye, S.; Wang, H.; Yan, H. Selection of Optimal Building Facade Texture Images From UAV-Based Multiple Oblique Image Flows. *IEEE Trans. Geosci. Remote Sens.* **2020**, *59*, 1534–1552. [[CrossRef](#)]
41. Huang, S.; Huang, M.; Lyu, Y. Seismic performance analysis of a wind turbine with a monopile foundation affected by sea ice based on a simple numerical method. *Eng. Appl. Comput. Fluid Mech.* **2021**, *15*, 1113–1133. [[CrossRef](#)]
42. Li, R.; Yu, N.; Wang, X.; Liu, Y.; Cai, Z.; Wang, E. Model-Based Synthetic Geoelectric Sampling for Magnetotelluric Inversion with Deep Neural Networks. *IEEE Trans. Geosci. Remote Sens.* **2020**, *60*, 4500514. [[CrossRef](#)]
43. Zhang, Y.; Luo, J.; Li, J.; Mao, D.; Zhang, Y.; Huang, Y.; Yang, J. Fast Inverse-Scattering Reconstruction for Airborne High-Squint Radar Imagery Based on Doppler Centroid Compensation. *IEEE Trans. Geosci. Remote Sens.* **2021**, *60*, 5205517. [[CrossRef](#)]
44. Xie, X.; Xie, B.; Cheng, J.; Chu, Q.; Dooling, T. A simple Monte Carlo method for estimating the chance of a cyclone impact. *Nat. Hazards* **2021**, *107*, 2573–2582. [[CrossRef](#)]
45. Xie, X.; Tian, Y.; Wei, G. Deduction of sudden rainstorm scenarios: Integrating decision makers' emotions, dynamic Bayesian network and DS evidence theory. *Nat. Hazards* **2022**, *45*, 5303435. [[CrossRef](#)]
46. Zhu, X.; Xu, Z.; Liu, Z.; Liu, M.; Yin, Z.; Yin, L.; Zheng, W. Impact of dam construction on precipitation: A regional perspective. *Mar. Freshw. Res.* **2022**, *63*, 23–32. [[CrossRef](#)]
47. Schaer, S. *Mapping and Predicting the Earth's Ionosphere Using the Global Positioning System*; Schweizerische Geodätische Kommission: Zürich, Switzerland, 1999; Volume 59.
48. Dobrovolsky, I.P.; Zubkov, S.I.; Miachkin, V.I. Estimation of the size of earthquake preparation zones. *Pure Appl. Geophys.* **1979**, *117*, 1025–1044. [[CrossRef](#)]
49. Akyol, A.A.; Arikan, O.; Arikan, F. A machine learning-based detection of earthquake precursors using ionospheric data. *Radio Sci.* **2020**, *55*, 1–21. [[CrossRef](#)]

50. Al Ibrahim, M.; Park, J.; Athens, N. *Earthquake Warning System: Detecting Earthquake Precursor Signals Using Deep Neural Networks*; Stanford University Press: Redwood City, CA, USA, 2018; p. 230.
51. Ouzounov, D.; Liu, D.; Chunli, K.; Cervone, G.; Kafatos, M.; Taylor, P. Outgoing long wave radiation variability from IR satellite data prior to major earthquakes. *Tectonophysics* **2007**, *431*, 211–220. [[CrossRef](#)]
52. Jing, F.; Shen, X.H.; Kang, C.L.; Xiong, P. Variations of multi-parameter observations in atmosphere related to earthquake. *Nat. Hazards Earth Syst. Sci.* **2013**, *13*, 27–33. [[CrossRef](#)]
53. Walker, R.; Jackson, J. Offset and evolution of the Gowk fault, SE Iran: A major intra-continental strike-slip system. *J. Struct. Geol.* **2002**, *24*, 1677–1698. [[CrossRef](#)]
54. Hereher, M.; Bantan, R.; Gheith, A.; El-Kenawy, A. Spatio-temporal variability of sea surface temperatures in the Red Sea and their implications on Saudi Arabia coral reefs. *Geocarto Int.* **2022**, *37*, 5636–5652. [[CrossRef](#)]
55. Shah, M.; Qureshi, R.U.; Khan, N.G.; Ehsan, M.; Yan, J. Artificial Neural Network based thermal anomalies associated with earthquakes in Pakistan from MODIS LST. *J. Atmos. Solar-Terrestrial Phys.* **2021**, *215*, 105568. [[CrossRef](#)]
56. Freund, F.T.; Takeuchi, A.; Lau, B.W.S.; Al-Manaseer, A.; Fu, C.C.; Bryant, N.A.; Ouzounov, D. Stimulated infrared emission from rocks: Assessing a stress indicator. *eEarth* **2007**, *2*, 7–16. [[CrossRef](#)]
57. Shah, M.; Abbas, A.; Ehsan, M.; Aiber, A.C.; Adhikari, B.; Tariq, M.A.; Ahmed, J.; de Oliveira-Júnior, J.F.; Yan, J.; Melgarejo-Morales, A.; et al. Ionospheric-thermospheric responses in south America to the august 2018 geomagnetic storm based on multiple observations. *IEEE J. Sel. Top. Appl. Earth Obs. Remote Sens.* **2021**, *15*, 261–269. [[CrossRef](#)]
58. Ondoh, T. Anomalous sporadic-E layers observed before M7.2 Hyogo-ken Nanbu earthquake; Terrestrial gas emanation model. *Adv. Polar Upper Atmos. Res.* **2003**, *17*, 96–108.
59. Tariq, M.A.; Shah, M.; Inyurt, S.; Shah, M.A.; Liu, L. Comparison of TEC from IRI-2016 and GPS during the low solar activity over Turkey. *Astrophys. Space Sci.* **2020**, *365*, 179. [[CrossRef](#)]
60. Yin, L.; Wang, L.; Tian, J.; Yin, Z.; Liu, M.; Zheng, W. Atmospheric Density Inversion Based on Swarm-C Satellite Accelerometer. *Appl. Sci.* **2023**, *13*, 3610. [[CrossRef](#)]
61. Liu, Z.; Xu, J.; Liu, M.; Yin, Z.; Liu, X.; Yin, L.; Zheng, W. Remote sensing and geostatistics in urban water-resource monitoring: A review. *Mar. Freshw. Res.* **2023**, *82*, 34–45. [[CrossRef](#)]
62. Zhang, S.; Bai, X.; Zhao, C.; Tan, Q.; Luo, G.; Wang, J.; Li, Q.; Wu, L.; Chen, F.; Li, C.; et al. Global CO₂ Consumption by Silicate Rock Chemical Weathering: It's past and Future. *Earth's Future* **2021**, *9*, e1938E–e2020E. [[CrossRef](#)]
63. Cheng, Y.; Fu, L.-Y. Nonlinear seismic inversion by physics-informed Caianiello convolutional neural networks for overpressure prediction of source rocks in the offshore Xihu depression, East China. *J. Pet. Sci. Eng.* **2022**, *215*, 110654. [[CrossRef](#)]
64. Shahzad, F.; Shah, M.; Riaz, S.; Ghaffar, B.; Ullah, I.; Eldin, S.M. Integrated Analysis of Lithosphere-Atmosphere-Ionospheric Coupling Associated with the 2021 Mw 7.2 Haiti Earthquake. *Atmosphere* **2023**, *14*, 347. [[CrossRef](#)]
65. Shah, M.; Shahzad, R.; Ehsan, M.; Ghaffar, B.; Ullah, I.; Jamjareegulgarn, P.; Hassan, A.M. Seismo Ionospheric Anomalies around and over the Epicenters of Pakistan Earthquakes. *Atmosphere* **2023**, *14*, 601. [[CrossRef](#)]

Disclaimer/Publisher's Note: The statements, opinions and data contained in all publications are solely those of the individual author(s) and contributor(s) and not of MDPI and/or the editor(s). MDPI and/or the editor(s) disclaim responsibility for any injury to people or property resulting from any ideas, methods, instructions or products referred to in the content.